Supplementary Information for Radiative properties of quantum emitters in boron nitride from excited state calculations and Bayesian analysis

Shiyuan Gao,[1] Hsiao-Yi Chen,[1,2] Marco Bernardi[1,*]

[1] *Department of Applied Physics and Material Science, California Institute of Technology, Pasadena, California 91125, USA*

[2] *Department of Physics, California Institute of Technology, Pasadena, California 91125, USA*

*To whom correspondence should be addressed; E-mail: bmarco@caltech.edu.

Supplementary Note 1

Convergence of the GW-BSE calculations The convergence of our GW-BSE calculations against the number of bands and the cutoff of dielectric matrix is checked using the V_NN_B defect in a 4×4 supercell as a prototypical case. As shown in Supplementary Table 1 below, the quasiparticle energy is converged for the 10 Ry cutoff energy and 800 bands (or 8 times the number of valence bands, for systems with different sizes) used in our calculations.

We also use the same prototype to check the convergence of the exciton state against the number of bands included in the BSE matrix. Supplementary Figure 1 below shows the absorption spectrum of the V_NN_B defect when different number of bands are included in the diagonalization of the BSE matrix. The main exciton peak around 2.4 eV is converged with just 9 bands (splitted 4/5 between valence and conduction bands for each spin). (Due to the smaller supercell used in this test, the exciton energy is different from the value reported in the manuscript.) Therefore, including at least 6 valence bands and 6 conduction bands in the BSE calculation can ensure convergence.

Finally, the convergence of our GW-BSE calculations is checked against the sizes of the supercell, **k**-point grid of the dielectric function and vacuum using the V_NC_B defect as a prototypical case. As shown in Supplementary Table 2, the exciton energy and transition dipole both reach a converged value for a 2×2×1 **k**-point grid, and thus the 3×3×1 **k**-point grid employed in our calculations is converged. Using a supercell size greater than 5×5 and increasing the vacuum beyond 1.5 nm does not change the GW band gap, exciton energies

converge with respect to	dielectric cutoff (Ry)	number of bands	VBM spin-down (eV)	VBM spin-up (eV)	CBM spin-down (eV)	CBM spin-up (eV)
dielectric cutoff	4	400	-1.44	0	4.55	4.92
	6		-1.58	0	4.27	4.71
	8		-1.63	0	4.23	4.70
	10		-1.67	0	4.18	4.66
	12		-1.69	0	4.16	4.65
number of bands	6	400	-1.58	0	4.27	4.71
		800	-1.57	0	4.22	4.64

Supplementary Table 1. Convergence of the GW calculations. The convergence of the GW quasiparticle energy with respect to the cutoff energy of the dielectric matrix and the total number of bands used for the polarizability and self-energy summation is shown. The $V_N N_B$ defect in a 4×4 supercell is used with a 3×3 k-point grid. The spin-up VBM energy is used as a reference.

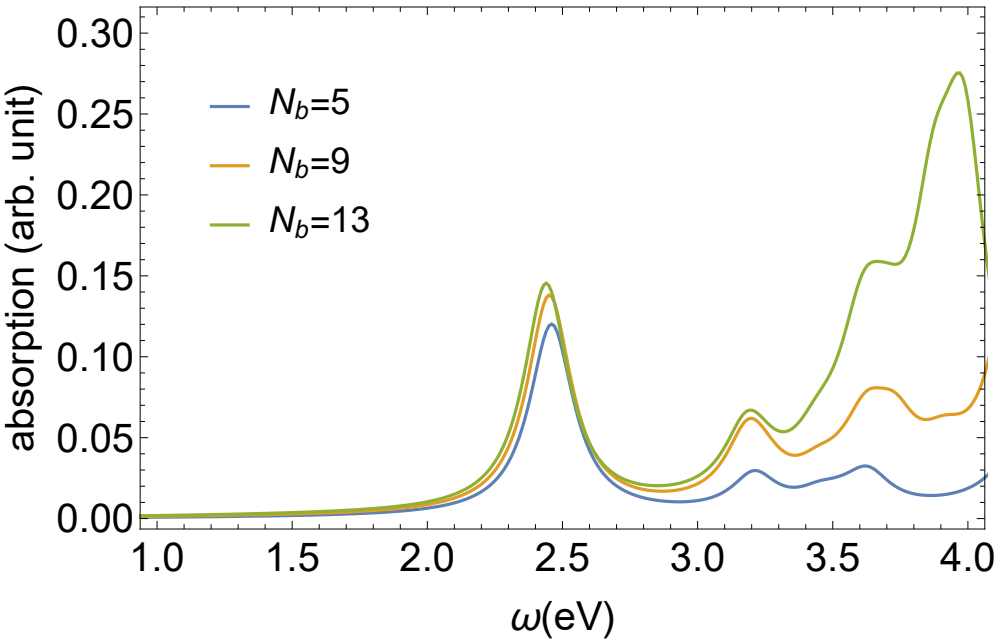

Supplementary Figure 1. Convergence of the optical absorption spectrum. Convergence of the optical absorption spectrum with respect to the number of bands N_b used in the BSE diagonalization is shown.

and transition dipoles appreciably. Therefore, our choice of working with 5×5 supercells and 1.5 nm vacuum guarantees reliable results. Although the GW band gap converges slower than the exciton energy with respect to the **k**-point grid, this trend does not affect the conclusions of our work. We believe this trend is due to the slow convergence of the long-range part of the screened Coulomb interaction in 2D materials[1], which makes approximately equal but

opposite contribution to the screened-exchange self-energy and exciton binding energy.

converge with respect to	supercell size	k-grid	vacuum size (nm)	GW band gap (eV)	lowest exciton energy (eV)	lowest exciton transition dipole (per k-point)
k-grid	5×5	1×1×1	1.5	5.92	2.44	0.175
	5×5	2×2×1	1.5	5.08	2.58	0.212
	5×5	3×3×1	1.5	4.86	2.61	0.214
	5×5	4×4×1	1.5	4.77	2.62	0.216
vacuum	5×5	2×2×1	2	5.09	2.59	0.210
supercell size	6×6	1×1×1	1.5	5.65	2.55	0.225
	6×6	2×2×1	1.5	5.01	2.63	0.222

Supplementary Table 2. Convergence of the GW-BSE calculations. Convergence of the GW-BSE calculations with respect to the sizes of the supercell, **k**-point grid and vacuum.

Supplementary Note 2

Properties of candidate defects Supplementary Table 3 below shows other properties of the candidate defect that are not included in the main text due to limitation in space, including the formation energy and the GW transition energy. Formation energy is calculated using $E_{\text{form}}[X] = E_{\text{tot}}[X] - E_{\text{tot}}[\text{hBN}] - \sum_i n_i \mu_i$ for defect X where n_i and μ_i is the number difference and chemical potential of atomic species i. The total energy of atoms in α-R boron, N_2 molecule, diamond and O_2 molecule are used as the reference for the chemical potential.

Supplementary Figure 2 below shows the optical absorption spectrum for all the hBN defect structures on which we carried out GW-BSE calculations. Shown are the absorption spectra calculated from the DFT electronic band energies, without including quasiparticle corrections or excitons (curves labeled "RPA"), as well as the absorption spectra including quasiparticle corrections but without excitons (GW-RPA curves) and the absorption spectra including both GW corrections and excitons (GW-BSE curves). The latter is the most accurate level of the theory and it was employed as input for our Bayesian approach.

type	defect	ground state spin polarization	formation energy (PBE, eV)	same-spin band gap (PBE, eV)	same-spin band gap (GW, eV)
native defect	V_B	3/2	9.8	0.66	
	N_B	0	6.9	2.32	
	V_N	1/2	7.4	2.05*	4.69
	B_N	0	7.0	2.20*	5.10
	V_NV_B	0	11.3	2.84	
	B_NV_B	1/2	7.4	0.85	
	V_NN_B	1/2	10.1	2.04	4.45
	B_NN_B	0	7.5	2.82	
	SW	0	7.0	3.57	6.24
carbon impurity	C_B	1.2	3.9	1.35	
	C_N	1/2	4.0	1.25	3.89
	C_NV_B	1	11.9	1.15	3.78
	C_NN_B	1/2	7.2	2.22	
	V_NC_B	0	9.6	1.93	4.86
	B_NC_B	1/2	7.2	2.3	
	C_NC_B	0	4.1	3.52	
oxygen impurity	O_B	1/2	7.5	1.51	4.47
	O_N	1/2	1.6	0	
	O_NV_B	1	5.4	0.72	3.72
	O_NN_B	1/2	5.9	2.3	
	V_NO_B	0	9.0	3.02	5.84
	B_NO_B	1/2	9.3	2.2	
	O_NO_B	0	4.6	3.41	

Supplementary Table 3. Calculated properties of candidate defect emitters. SW is the Stone-Wales defect. The * symbol marks the cases where we exclude lower band gaps with a symmetry-forbidden dipole transition.

Supplementary Note 3

Details of the Bayesian inference process In the Bayesian inference method, a posterior likelihood $p(h|E)$ of a given hypothesis h (here a hypothetical atomic structure of the emitter) is derived from the product of the prior likelihood $p(h)$ and the likelihood function

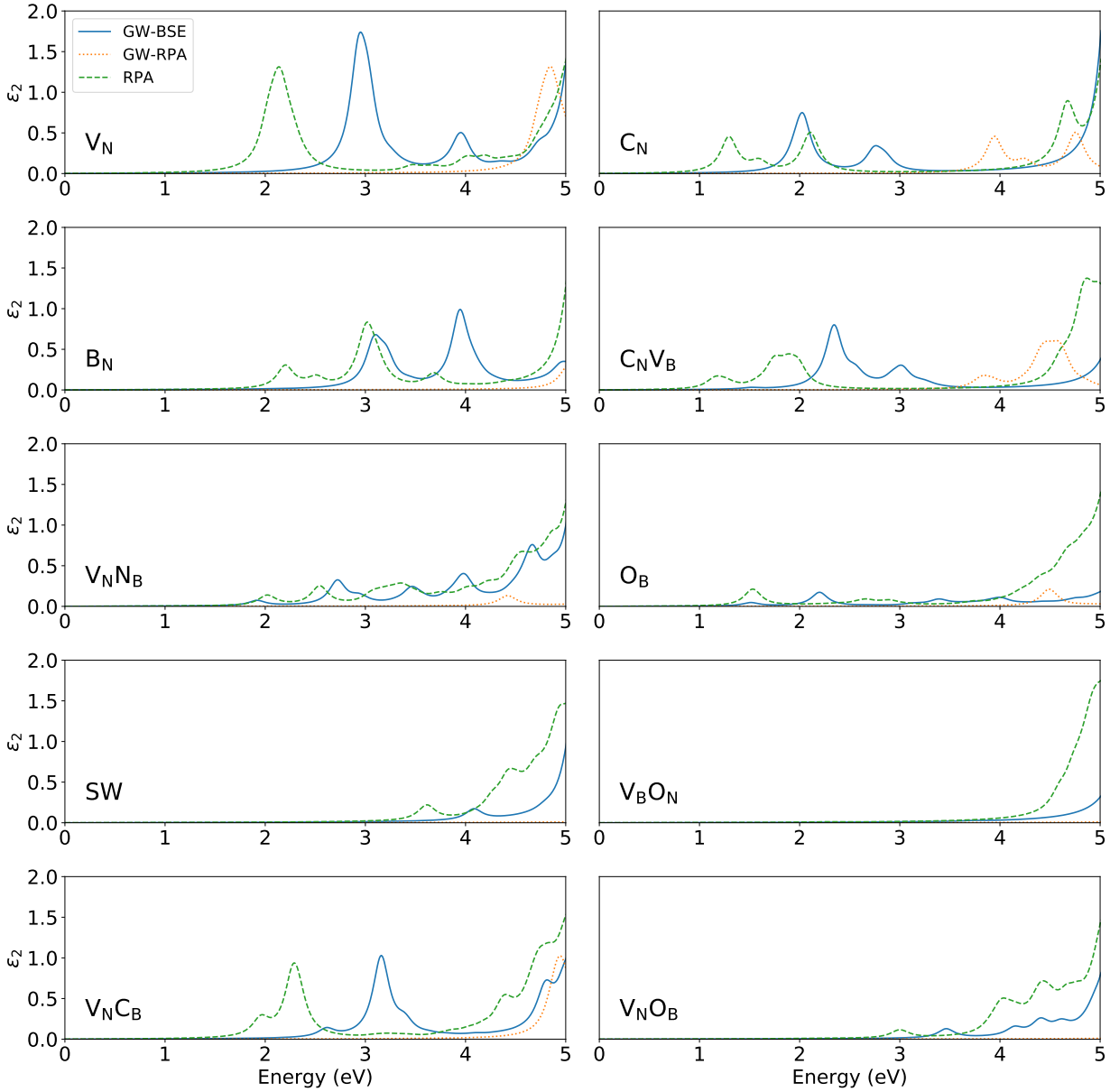

Supplementary Figure 2. The optical absorption spectrum of hBN defect structures from GW-BSE calculations. The absorption is expressed as the imaginary part of the dielectric constant ε_2. SW is the Stone-Wales defect.

$p(E|h)$ that describes how well the evidence E matches the hypothesis:

$$p(h|E) \propto p(h)p(E|h). \tag{1}$$

The likelihood here is employed to infer which structures are more likely among those considered. Note that the likelihood is meaningful only for comparisons within the pool of structures considered; it does not represent the probability of a certain defect structure being the "true" structure, and it is not normalized to 1. To carry out the Bayesian inference

procedure, three elements need to be specified: the set H from which the hypothesis h is drawn, the method to determine the prior $p(h)$, and the method to determine the likelihood function $p(E|h)$. In our study, we choose these elements as follows:

1. While the number of possible structures is in principle unlimited, here we generate the set H of candidate point defect structures by enumerating defects according to the number of sites they occupy. Each atomic site in the original hBN lattice can be replaced by a vacancy (V_B, V_N), an antisite atom (N_B, B_N) or a substitutional impurity element (e.g. C_B, C_N). The possible structures in which multiple atomic sites are replaced are generated from the combination of these one-site replacements. Here we investigate all charge-neutral native defects and carbon/oxygen impurities that occupy one or two adjacent atomic sites. These structures span most defect emitters of interest in hBN[2–9], with exception of non-hexagonal lattice reconstructions such as the Stone-Wales (SW) defect, dislocations and other more extended defects with three or more atomic replacements. We have verified in Fig. S1 above that the SW defect exhibits emission energies of order 4 eV and thus well outside the range of interest (1.6−2.2 eV) in this work. Interstitial defects, which are similarly not included in our analysis, have been shown to possess a low migration barrier and become unstable at room temperature in hBN[5], contrary to the experimental observation that the SPEs in hBN remain stable well above room temperature[10]. Finally, we have not included defects that appear along the edge, such as the boron dangling bond[11], which may account for some of the emitters in hBN[12–15].

2. The prior likelihood $p(h)$ represents the probability for defect h to exist in the hBN sample a priori, without considering the measured properties of the emitter. In general, $p(h)$ is determined by the formation process of the defect, often out of thermal equilibrium, which depends on many factors that are generally difficult to quantify, such as the sample preparation procedure and the chemical composition and stability of the defect. Here, we make the assumption that more complex structures or structures that involve external elements are less common than simpler structures and native defects. The prior likelihood for each defect is assumed to take a single exponential form:

$$p(h) \propto S_h A^{-C_h}, \tag{2}$$

where C_h is a "complexity index" of the structure h, defined as the number of vacancies and antisites plus twice the number of impurities in the structure, A is a constant to be determined below, and S_h is a degeneracy factor accounting for symmetry-related configurations.

The advantage of this model is that the only free parameter A can be determined using the maximum entropy principle[16], which states that the prior probability distribution should contain minimal information beyond what the model requires, and thus maximize the entropy $S = -\sum_{h\in H} p(h)\log(p(h))$, where H is the set of all possible structures. Using the ansatz that $p(h)$ takes the form in Eq.(2), the only constraint we impose is that the total probability, summed over all possible structures (as the number of sites in the structures go to infinity) converges to a finite number and therefore is normalizable. This normalizability is achieved here by finding the minimal value of A that converges the series $\sum_{C\to\infty} N(C)A^{-C}$, where $N(C)$ is the number of different configurations with "complexity index" C. To this end, we use the numerical result that the number of different clusters on a honeycomb lattice grows exponentially with the size of the cluster[17], obtaining a minimum $A \approx 3.8$ for the series to converge, which we use to calculate our prior likelihood.

3. The likelihood function $p(E|h)$ is determined by comparing the results of our ab initio calculations for each structure H with available experimental results for the emitters, as discussed in the main text. The posterior likelihood based on DFT results are determined from the DFT transition energy and polarization of the emission: $p_1(h|E) = p(h)p_{\mathrm{DFT}}(E|h)p_{\mathrm{pol}}(E|h)$, and those based on GW-BSE results are determined from the GW-BSE transition energy and radiative lifetime of the emission, plus the polarization information gained from DFT results: $p_2(h|E) = p(h)p_{\mathrm{pol}}(E|h)p_{\text{GW-BSE}}(E|h)p_{\mathrm{lifetime}}(E|h)$. To compare the transition energy with experiment, we assume, for a given calculated transition energy ε_h for defect h, that the value of the real transition energy of the defect has a normal probability distribution $N(\varepsilon_h, \sigma^2)$ centered around ε_h, where σ is the standard deviation, which depends on the accuracy of the calculation method. To account for the range of experimental values, we use $p_{\text{DFT/GW-BSE}}(E|h) = N(\varepsilon_h, \sigma^2) \cdot \mathrm{unif}(\varepsilon_E^1, \varepsilon_E^2)$, where $\mathrm{unif}(\varepsilon_E^1, \varepsilon_E^2)$ is the uniform distribution function between energies ε_E^1=1.6 eV and ε_E^2=2.2 eV, which defines the energy range in which SPEs are observed experimentally, and the dot product stands for integrating the product of the two functions. Using our calculated GW-BSE results for all the hBN defects as benchmark, we determine the standard deviation of the DFT transition energy to be 0.45 eV. For the GW-BSE calculations, we assume a standard deviation of 0.2 eV, based on a conservative estimate of the accuracy (10% of the band gap) of the method for typical band gap values of semiconductors and insulators[18].

In addition to the transition energy, the emission polarization and radiative lifetime are also included in the inference process. The likelihood function $p_{\mathrm{pol}}(E|h)$ is set to zero for defects with D_{3h} symmetry because they will not emit polarized light and thus should be excluded, while it is set to one for defects with other symmetries. Our computed radiative lifetime values are greater than the experimental lifetimes; as discussed in the main text, this trend is attributed to non-radiative decay channels that may reduce the quantum yield of the emitters measured in experiments. Despite this, longer radiative lifetimes correspond to dimmer emitters, which cannot account for the bright SPEs seen in experiment. Therefore, we set a likelihood function for radiative lifetime that halves with every order of magnitude difference between the experimental lifetime τ_E and calculated lifetime τ_h: $p_{\mathrm{lifetime}}(E|h) = 2^{-log_{10}(\tau_h/\tau_E)}$, where the experimental lifetime τ_E is chosen as 10 ns, which is approximately the upper bound of the reported experimental values.

References

[1] D. Y. Qiu, F. H. da Jornada, S. G. Louie, Screening and many-body effects in two-dimensional crystals: Monolayer mos_2. *Phys. Rev. B* **93**, 235435 (2016).

[2] S. A. Tawfik, S. Ali, M. Fronzi, M. Kianinia, T. T. Tran, C. Stampfl, I. Aharonovich, M. Toth, M. J. Ford, First-principles investigation of quantum emission from hBN defects. *Nanoscale* **9**, 13575–13582 (2017).

[3] M. Abdi, J. P. Chou, A. Gali, M. B. Plenio, Color centers in hexagonal boron nitride monolayers: a group theory and ab initio analysis. *ACS Photonics* **5**, 1967–1976 (2018).

[4] A. Sajid, J. R. Reimers, M. J. Ford, Defect states in hexagonal boron nitride: Assignments of observed properties and prediction of properties relevant to quantum computation. *Phys. Rev. B* **97**, 1–9 (2018).

[5] L. Weston, D. Wickramaratne, M. Mackoit, A. Alkauskas, C. G. Van De Walle, Native point defects and impurities in hexagonal boron nitride. *Phys. Rev. B* **97**, 1–13 (2018).

[6] J. R. Reimers, A. Sajid, R. Kobayashi, M. J. Ford, Understanding and calibrating density-functional-theory calculations describing the energy and spectroscopy of defect sites in hexagonal boron nitride. *J. Chem. Theory Comput.* **14**, 1602–1613 (2018).

[7] G. I. López-Morales, N. V. Proscia, G. E. López, C. A. Meriles, V. M. Menon, Toward the identification of atomic defects in hexagonal boron nitride: X-Ray photoelectron spectroscopy and first-principles calculations. *Preprint at arXiv:1811.05924* .

[8] G. Noh, D. Choi, J. H. Kim, D. G. Im, Y. H. Kim, H. Seo, J. Lee, Stark tuning of single-photon emitters in hexagonal boron nitride. *Nano Lett.* **18**, 4710–4715 (2018).

[9] V. Ivády, G. Barcza, G. Thiering, S. Li, H. Hamdi, J.-P. Chou, Ö. Legeza, A. Gali, Ab initio theory of the negatively charged boron vacancy qubit in hexagonal boron nitride. *npj Computational Materials* **6** (2020).

[10] N. R. Jungwirth, B. Calderon, Y. Ji, M. G. Spencer, M. E. Flatté, G. D. Fuchs, Temperature dependence of wavelength selectable zero-phonon emission from single defects in hexagonal boron nitride. *Nano Lett.* **16**, 6052–6057 (2016).

[11] M. E. Turiansky, A. Alkauskas, L. C. Bassett, C. G. Van De Walle, Dangling bonds in hexagonal boron nitride as single-photon emitters. *Phys. Rev. Lett.* **123**, 127401 (2019).

[12] A. L. Exarhos, D. A. Hopper, R. R. Grote, A. Alkauskas, L. C. Bassett, Optical signatures of quantum emitters in suspended hexagonal boron nitride. *ACS Nano* **11**, 3328–3336 (2017).

[13] N. Chejanovsky, M. Rezai, F. Paolucci, Y. Kim, T. Rendler, W. Rouabeh, F. Fávaro De Oliveira, P. Herlinger, A. Denisenko, S. Yang, I. Gerhardt, A. Finkler, J. H. Smet, J. Wrachtrup, Structural attributes and photodynamics of visible spectrum quantum emitters in hexagonal boron nitride. *Nano Lett.* **16**, 7037–7045 (2016).

[14] S. Choi, T. T. Tran, C. Elbadawi, C. Lobo, X. Wang, S. Juodkazis, G. Seniutinas, M. Toth, I. Aharonovich, Engineering and localization of quantum emitters in large hexagonal boron nitride layers. *ACS Appl. Mater. Interfaces* **8**, 29642–29648 (2016).

[15] F. Hayee, L. Yu, J. L. Zhang, C. J. Ciccarino, M. Nguyen, A. F. Marshall, I. Aharonovich, J. Vučković, P. Narang, T. F. Heinz, J. A. Dionne, Revealing multiple classes of stable quantum emitters in hexagonal boron nitride with correlated optical and electron microscopy. *Nat. Mater.* **19**, 534–539 (2020).

[16] U. Von Toussaint, Bayesian inference in physics. *Rev. Mod. Phys.* **83**, 943–999 (2011).

[17] M. F. Sykes, M. Glen, Percolation processes in two dimensions. I. Low-density series expansions. *J. Phys. A: General Physics* **9**, 87–95 (1976).

[18] G. Onida, L. Reining, A. Rubio, Electronic excitations: Density-functional versus many-body Green's-function approaches. *Rev. Mod. Phys.* **74**, 601–659 (2002).